

Nanoarray heterojunction and its efficient solar cells without negative impact of photogenerated electric field

Rong Liu^{1,2,5}, Zhitao Shen^{3,5}, Zhiyang Wan^{1,2,5}, Liangxin Zhu^{1,2}, Junwei Chen¹✉, Chao Dong¹, Wangwei Chen^{1,2}, Wenbo Cao^{1,2}, Bin Chen¹, Xiaogang Yuan^{2,4}, Bojiang Ding⁴, Shangfeng Yang², Tao Chen², Xingyou Tian¹, Chong Chen³✉ & Mingtai Wang¹✉

Efficient, stable and low-cost solar cells are being desired for the photovoltaic conversion of solar energy into electricity for sustainable energy production. Nanorod/nanowire arrays of narrow-bandgap semiconductors are the promising light-harvesters for photovoltaics because of their excellent optoelectrical properties. Here, the array of preferentially oriented antimony trisulfide (Sb_2S_3) single-crystalline nanorods is grown on polycrystalline titania (TiO_2) film by a tiny-seed-assisted solution-processing strategy, offering an $\text{Sb}_2\text{S}_3/\text{TiO}_2$ nanoarray heterojunction system on a large scale. It is demonstrated that the Sb_2S_3 nanorod growth follows a tiny-seed-governed orientation-competing-epitaxial nucleation/growth mechanism. Using a conjugated polymer hole transporting layer on the heterojunction, we achieve a power conversion efficiency of 5.70% in the stable hybrid solar cell with a preferred p-type/intrinsic/n-type architecture featuring effectively straightforward charge transport channels and no negative impact of photogenerated electric field on device performance. An architecture-dependent charge distribution model is proposed to understand the unique photovoltaic behavior.

¹Institute of Solid State Physics, HFIPS, Chinese Academy of Sciences, Hefei, China. ²University of Science and Technology of China, Hefei, China. ³Henan Key Laboratory of Photovoltaic Materials, Henan University, Kaifeng, China. ⁴Institute of Plasma Physics, HFIPS, Chinese Academy of Sciences, Hefei, China. ⁵These authors contributed equally: Rong Liu, Zhitao Shen, Zhiyang Wan. ✉email: jwchen@issp.ac.cn; chongchen@henu.edu.cn; mtwang@ipp.ac.cn

Photovoltaic technology is one of the promising ways to solve the problems of energy demand, and efficient, stable, low-cost, and non-toxic solar cells are being desired for the conversion of solar energy into electricity. With the excellent properties, such as photon absorption through coupling effect, straightforward pathways for charge carrier transport, and defined optoelectrical property by tailored structure, the nanorods/nanowires of narrow-bandgap semiconductors have attracted intensive attention to their photovoltaic applications^{1–4}. Many narrow-bandgap nanorod/nanowire arrays have been used as light-harvesting materials in solar cells, including silicon^{1,2} and III–V compounds (e.g., GaAs, GaN, InP)^{5–7}. Amongst the III–V compounds, axial and radial p–n^{5,7–9} or p–intrinsic–n (p–i–n)^{5–7,10,11} junction nanorods/nanowires are generally designed for those nanorod/nanowire arrays in order to obtain high photovoltaic performance. An axial p–n or p–i–n junction nanorod/nanowire is normally created by changing doping states along the axis direction of the nanorod/nanowire, while a radial p–n or p–i–n junction nanorod/nanowire is often obtained by forming a core-shell structure along the radial direction of the nanorod/nanowire due to the different doping states for example. However, the preparation of those p–n and p–i–n junction nanorod/nanowire arrays usually involves sophisticated chemical vapor deposition and molecular beam epitaxy technologies.

Growing the nanorod/nanowire array of intrinsic narrow-bandgap semiconductor (A) on the film of n-type semiconductor (B) renders a material system, which is here referred to as a nanoarray heterojunction (NHJ) since individual A/B heterojunctions are actually resulted upon the contact between each of A nanorods and the beneath B film and the A/B-NHJ property correlates tightly to the discontinuous and nanosized A/B heterojunctions (i.e., A/B interfaces). On one hand, the NHJ is quite different from the p–n and p–i–n junction nanorod/nanowire arrays in that the properties of the latter two arrays are mainly determined by the p–n and p–i–n junction nanorod/nanowires. On the other hand, the A/B-NHJ is also essentially different from the planar heterojunction (PHJ) formed by sequentially depositing A compact film onto B film (A/B-PHJ). The A/B-NHJ has many discontinuous and nanosized A/B interfaces for interfacial charge generation and transportation due to the interspaces in between nanorods, but the A/B-PHJ has only one two-dimensional and micro-/macro-sized A/B interface for interfacial charge behaviors. Moreover, when combining with a third material C, the A/B-PHJ only offers an A surface to form another new PHJ with a two-dimensional interface of A and C components and results in a ternary C/A/B-PHJ derivative system, while the A/B-NHJ has many side-faces and top-faces of A nanorods/nanowires to form a bulk heterojunction (BHJ) with three-dimensionally distributed A/C interfaces and yields an integrated C/A/B derivative of two-dimensional PHJ and three-dimensional BHJ structures. Therefore, the distinct structural characteristics of the NHJ and PHJ will inevitably lead to the different optoelectrical and photophysical properties of themselves and their derivatives. In short, the NHJ represents a kind of heterojunction formation and is quite different from the PHJ and the p–n or p–i–n junction nanorod/nanowire array. The NHJs formed by the nanorods/nanowires of narrow-bandgap semiconductors on wide-bandgap semiconductors (e.g., TiO₂, ZnO) films should be of great interest for photovoltaic application in that they combine together the good absorption and straightforward charge transport channels, but their preparation still remains a challenge.

Antimony trisulfide (Sb₂S₃) is a promising photon-harvesting candidate for solar cells because of its narrow and direct bandgap (~1.4–1.8 eV) matching well the solar spectrum, high absorption coefficient (~10⁵ cm⁻¹), excellent air/moisture

stability, non-toxicity, earth-abundant elemental composition, and easy preparation¹². The Sb₂S₃-based single-junction solar cells are theoretically expected to achieve the efficiency of $\eta = 27\text{--}33\%$ according to Shockley–Queisser limit¹³. Sb₂S₃ nanoparticle-sensitized solar cells have exhibited a record efficiency of $\eta = 7.5\%$ ¹⁴. Moreover, the Sb₂S₃ nanoparticle^{15–17} or bulk^{18,19} films as a photon-harvesting layer in planar heterojunction solar cells have achieved the efficiencies of 5.69–6.78% and 3.50–5.12%, respectively. Sb₂S₃ crystals comprise the (Sb₄S₆)_n ribbons that grow along [001] direction via strong covalent Sb–S bonds and are packed together along [100] and [010] directions by van der Waals forces (Inset to Fig. 1), and therefore Sb₂S₃ often features a one-dimensional crystalline structure and highly anisotropic properties along different axes. While the one-dimensional nanostructures of Sb₂S₃ nanorods/nanowires have been prepared by different methods²⁰, no reports on the growth of Sb₂S₃ nanorod/nanowire arrays are available up to now.

In this work, we develop a tiny-seed-assisted repetition of spin-coating and annealing (RSCA) strategy for preparing preferentially [211]-oriented and vertically aligned Sb₂S₃ single-crystalline nanorods on polycrystalline TiO₂ nanoparticle film, yielding an Sb₂S₃/TiO₂-NHJ, for which an epitaxial nucleation/growth mechanism gets revealed for the Sb₂S₃ nanorod growth. After depositing a conjugated polymer layer onto the Sb₂S₃/TiO₂-NHJ, a stable hybrid solar cell with p–i–n architecture is obtained and exhibits a considerable efficiency of 5.70%. It is found that, furthermore, there is no negative impact of photogenerated electric field (E_{ph}) on photovoltaic performance in such p–i–n solar cells, and an electric field distribution model is suggested for understanding the distinguishing photovoltaic feature.

Noticeably, we previously developed a seed-assisted RSCA method for preparing the monolayer of [221]-oriented bulk Sb₂S₃ single-crystalline cuboids on polycrystalline TiO₂ nanoparticle film¹⁹, where [211]/[221]-oriented Sb₂S₃ crystalline seeds laterally of 60–400 nm in size were deposited on the TiO₂ film prior to the RSCA cycles for Sb₂S₃ crystal growth, and an orientation-competing-epitaxial (OCE) nucleation/growth mechanism was proposed for the [221]-oriented Sb₂S₃ cuboid growth. In this work, we use the tiny [211]/[221]-oriented Sb₂S₃ crystalline seeds of laterally <10 nm in size to perform the seed-assisted RSCA process and obtain the [211]-oriented Sb₂S₃ single-crystalline nanorod array on the polycrystalline TiO₂ nanoparticle film. Our results demonstrate that the Sb₂S₃ nanorod growth follows a tiny-seed-governed OCE nucleation/growth mechanism, where the tiny size of Sb₂S₃ seeds is exclusively important to govern the orientation and morphology of resulting Sb₂S₃ nanorods. Undoubtedly, in regard to the heterojunction preparation, the insights in this work make significant advances in expanding the knowledge on the seed-assisted RSCA method and the OCE nucleation/growth mechanism.

Results

Preparation strategy. For simplicity, the Sb₂S₃ precursor solutions for Sb₂S₃ seed growth (SG) and nanorod growth (NG) are referred to as SG and NG solutions, respectively. The SG and NG solutions have the same composition and their concentrations (C_{sg} and C_{ng}) are defined by the molecular concentration of SbCl₃ therein. For the growth of the Sb₂S₃ nanorod array, C_{ng} must be much higher than C_{sg} , as indicated by solution color (Bottles 1 and 2, inset to Fig. 1). As shown in Fig. 1, an Sb₂S₃ precursor film is spin-coated from an NG solution onto the TiO₂ nanoparticle film decorated with oriented Sb₂S₃ crystalline seeds and then annealed in N₂ atmosphere at 300 °C, which is referred to as one RSCA cycle number (n); the Sb₂S₃/TiO₂-NHJ is produced after a certain

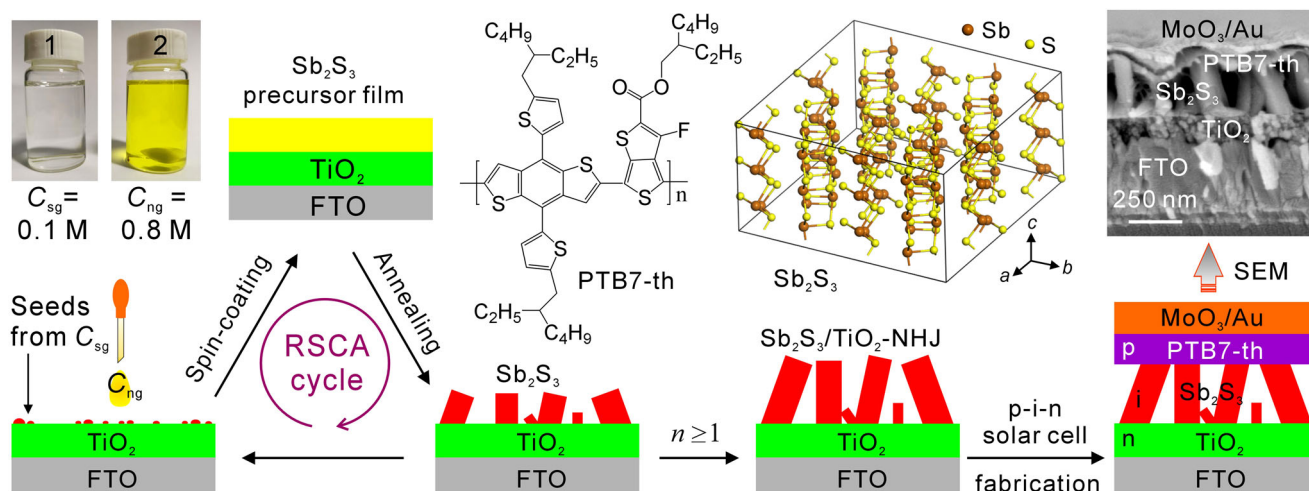


Fig. 1 Tiny-seed assisted repetition of spin-coating and annealing (RSCA) method, structures of materials, and device. The schematic illustration shows the preparation of the $\text{Sb}_2\text{S}_3/\text{TiO}_2$ -nanoarray heterojunction ($\text{Sb}_2\text{S}_3/\text{TiO}_2$ -NHJ) by a tiny-seed-assisted RSCA method on fluorine-doped tin oxide (FTO) substrate and the structure of p-i-n solar cell, where p means p-type PTB7-th, i means intrinsic Sb_2S_3 and n means n-type TiO_2 . The insets show the photographs of seed growth (bottle 1, colorless) and nanorod growth (bottle 2, yellow) solutions, the molecular structures of PTB7-th, the crystal structure of orthorhombic Sb_2S_3 , and the cross-sectional scanning electron microscopy (SEM) characterization of a practical p-i-n cell. Normally, the seed growth solution concentration of $C_{\text{sg}} = 0.1 \text{ M}$ and the nanorod growth solution concentration of $C_{\text{ng}} = 0.8 \text{ M}$ were, respectively, used for growing the Sb_2S_3 seeds prior to the RSCA cycles and the Sb_2S_3 nanorods in the RSCA cycles, unless otherwise specified. During the RSCA method, each of the precursor film formations by spin-coating followed by once annealing is referred to as one RSCA cycle for the nanorod growth, and the nanorod length (i.e., nanorod array thickness) is mainly controlled by the RSCA cycle number (n).

RSCA cycle numbers (i.e., $n \geq 1$). By coating a poly[4,8-bis(5-(2-ethylhexyl) thiophen-2-yl)benzo[1,2-b;4,5-b']dithiophene-2,6-diyl-alt-(4-(2-ethylhexyl)-3-fluorothieno[3,4-b]thiophene-)-2-carboxylate-2-6-diyl)] (PTB7-th, inset to Fig. 1) layer, we obtain a p-i-n hybrid solar cell with the spatially separated intrinsic Sb_2S_3 nanorods sandwiched between p-type PTB7-th hole transporting layer (HTL) and n-type TiO_2 electron transporting layer (ETL), and scanning electron microscopy (SEM) image (Inset to Fig. 1) clearly confirms the p-i-n architecture.

Characterization of nanorod array. SEM images (Fig. 2a, b) show that a large-area Sb_2S_3 layer is grown on the TiO_2 film and consists of the Sb_2S_3 nanorods that are of a right square prism shape, 50–150 nm in width, ca. 320 nm in length, and a number density (i.e., the number of the different nanorods per unit area) of ca. $36 \mu\text{m}^{-2}$ on the TiO_2 nanoparticle (ca. 10–20 nm in diameter) film of ca. 110 nm in thickness. Clearly, the Sb_2S_3 nanorods are grown along the directions out of substrate planes (i.e., out-of-plane growth) with the growth direction tilting some angles from the normal of TiO_2 film, resulting in an Sb_2S_3 nanorod array on the TiO_2 film. Fig. 2c shows the transmission electron microscopy (TEM) image of a single Sb_2S_3 nanorod of ca. 50 nm in width. Both selected area electron diffraction pattern and high-resolution TEM (HRTEM) image (Insets to Fig. 2c) clearly show that the nanorod is single-crystalline in nature and grows along [001] direction, where the HRTEM image exhibits the lattice fringes of 0.35 nm and 0.38 nm in spacing corresponding, respectively, to the (111)/($\bar{1}\bar{1}\bar{1}$) and (001) planes of orthorhombic Sb_2S_3 under [110] viewing direction. X-ray diffraction (XRD) results (Fig. 2d) show that the Sb_2S_3 nanorods exhibit the patterns of orthorhombic Sb_2S_3 (stibnite) (JCPDS No.42-1393), and are preferentially oriented with [211] direction normal to substrate plane (i.e., [211]-oriented) with the intensity (I) ratio of $I_{(211)}/I_{(130)} = 2.20$, much larger than the $I_{(211)}/I_{(130)} = 0.82$ for the powder sample, indicating that most of the nanorods have the out-of-plane growths along [001], [010], and [100] directions with (001), (100), and (010) planes tilting the average

angles of ca. 37° , 57° , and 74° on substrate plane, respectively (Inset to Fig. 2d). Moreover, the TiO_2 film on fluorine-doped tin oxide (FTO) substrate exhibits the strongest XRD peak of (101) plane of anatase TiO_2 (101) planes (Fig. 2d), inferring that the (101) crystal planes of TiO_2 nanoparticles exposed on the film surface orient in the direction parallel to substrate plane^{19,21}.

Growth mechanism of nanorod array. When Sb_2S_3 seeds are absent from the TiO_2 film, only the large and irregular Sb_2S_3 grains without a preferential orientation are obtained (Supplementary Fig. 1). Clearly, the Sb_2S_3 crystalline seeds are very crucial for the growth of the Sb_2S_3 nanorod array. Our results show that the TiO_2 film surface undoubtedly is decorated by the preferentially [211]/[221]-oriented Sb_2S_3 crystalline seeds that are of a C_{sg} -dependent size in the range of $C_{\text{sg}} = 0.05\text{--}0.4 \text{ M}$ (Supplementary Fig. 2 and Supplementary Note 1), where the [211]/[221]-oriented Sb_2S_3 seeds of irregular shapes (laterally ca. 60–450 nm) derived from $C_{\text{sg}} = 0.4 \text{ M}$ are clearly observed and similar to our previous observations¹⁹, but the [211]/[221]-oriented Sb_2S_3 seeds from $C_{\text{sg}} = 0.05\text{--}0.2 \text{ M}$ are not observable under SEM. Hence, the [211]/[221]-oriented seeds formed at $C_{\text{sg}} \leq 0.2 \text{ M}$ are very tiny and must be $< 10 \text{ nm}$ in size as evaluated from the SEM resolution.

In order to get insights into the growth mechanism for the Sb_2S_3 nanorod array on TiO_2 film, the dependences of the Sb_2S_3 nanorod growth on the conditions (C_{sg} , C_{ng} , and n) for the seed-assisted RSCA method are investigated. We find that the formation of [211]-oriented Sb_2S_3 nanorod array depends exclusively on the C_{sg} concentration, and the tiny [211]/[221]-oriented Sb_2S_3 seeds derived from a dilute SG solution of $C_{\text{sg}} \leq 0.1 \text{ M}$ are indispensable (Supplementary Fig. 3 and Supplementary Note 2); moreover, both C_{ng} and n in the ranges of $C_{\text{ng}} < 1.1 \text{ M}$ and $n < 3$ imposes no remarkable influences on the lateral size of Sb_2S_3 nanorods, but the lateral size of Sb_2S_3 nanorods gets dramatically increased to make an exception when both $C_{\text{ng}} = 1.1 \text{ M}$ and $n = 3$ (Supplementary Fig. 4 and Supplementary Note 3). Here, we mainly show the length and number density of Sb_2S_3 nanorods dependent on C_{ng} and n values. The increase in

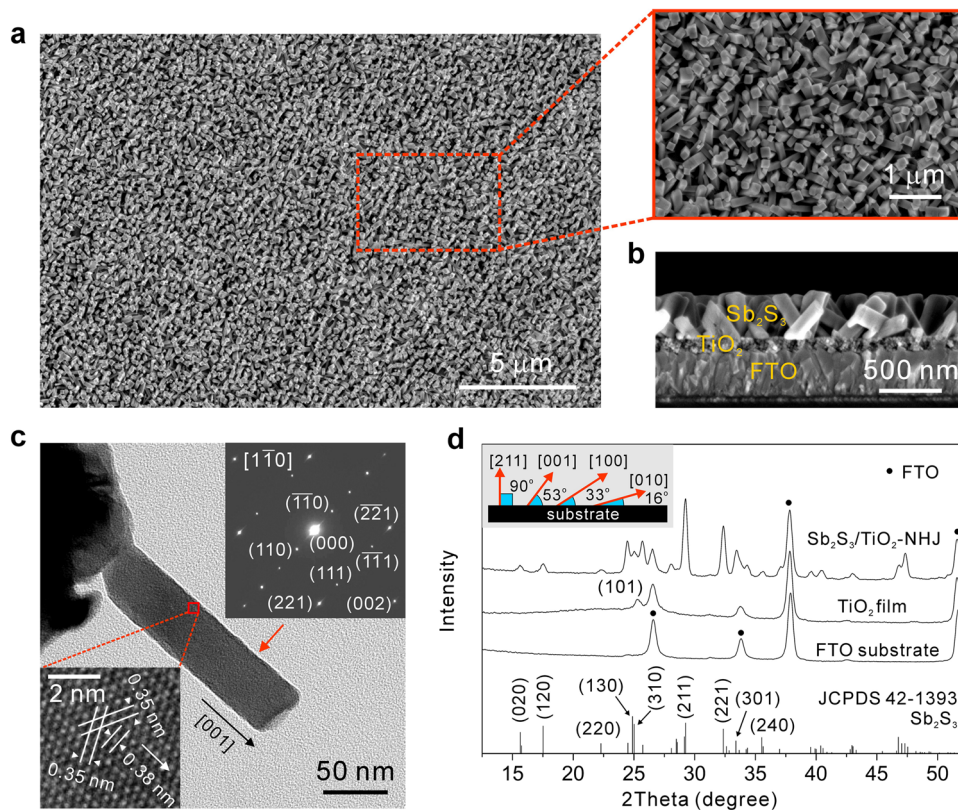


Fig. 2 Characterization of the Sb_2S_3 nanorod array grown on TiO_2 film. **a** Bird-view and **(b)** cross-sectional scanning electron microscopy images, **(c)** transmission electron microscopy (TEM) image, and **(d)** X-ray diffraction patterns. The insets to **c** are the selected area electron diffraction pattern (top-right) of the nanorod and the high-resolution TEM image from the marked part of the nanorod (bottom-left). Shown by the inset to **d**, the angle between a specific Sb_2S_3 crystal plane and the substrate is derived from the angle between the crystal plane and the Sb_2S_3 [211] direction that is normal to the substrate plane. The Sb_2S_3 nanorod array is prepared at the seed growth solution concentration of $C_{\text{sg}} = 0.1$ M, the nanorod growth solution concentration of $C_{\text{ng}} = 0.8$ M, and the repetition of spin-coating and annealing cycle number of $n = 2$.

either C_{ng} or n leads to the Sb_2S_3 nanorod growth along c -axis (i.e., a larger array thickness) (Fig. 3a). However, for $C_{\text{ng}} < 1.1$ M and $n < 3$, the number density is mainly affected by C_{ng} , and an increased C_{ng} results in a significantly reduced number density (Fig. 3b). Actually, the number density of Sb_2S_3 nanorods in most cases is not remarkably changed with n value, strongly indicating that the Sb_2S_3 nanorods mainly take a self-nucleated growth similar to the Sb_2S_3 cuboid growth¹⁹.

The growth of Sb_2Se_3 nanorod arrays on selenized Mo substrate by sublimation technique was proposed to follow a split growth model on the basis of the morphology transition from thin film to nanorod array when the lateral stress of the Sb_2Se_3 grains was beyond the tolerance of the van der Waals forces between $(\text{Sb}_4\text{Se}_6)_n$ ribbons during Sb_2Se_3 vapor evaporates²². Besides, quasi-epitaxial growth and dual-selection growth models were proposed, respectively, to elucidate the formation of $[hk1]$ -oriented Sb_2S_3 compact films on TiO_2 ²³ and CdS ²⁴ nanoparticle films. Unfortunately, there is no growth mechanism for the formation of Sb_2S_3 single-crystalline nanorods on polycrystalline surfaces. We previously proposed an OCE nucleation/growth mechanism to describe the growth of the Sb_2S_3 cuboids on polycrystalline TiO_2 film¹⁹. In the OCE nucleation/growth mechanism, the epitaxial relationship of Sb_2S_3 (101)// TiO_2 (101) exists for the heterogeneous nucleation of orthorhombic Sb_2S_3 crystal on favorably oriented anatase TiO_2 nanoparticle surface as the result of the lattice match between Sb_2S_3 (101) and TiO_2 (101) planes.

Known from the experimental evidence (Supplementary Fig. 5 and Supplementary Note 4), the growth of the [211]-oriented

Sb_2S_3 nanorods essentially follows an OCE nucleation/growth mechanism that is similar to that proposed for the growth of [221]-oriented Sb_2S_3 cuboids¹⁹. As shown by calculated results (Supplementary Table 1, Supplementary Fig. 6 and Supplementary Note 5), a TiO_2 nanoparticle theoretically needs to orientate with its (101) plane tilting in an angle range of $0^\circ \leq \alpha < 45^\circ$ on TiO_2 film plane in order to act as an effective epitaxial nucleation site for the out-of-plane growths of [211]-oriented Sb_2S_3 crystals along [001], [100], and [010] directions; moreover, considering the fact that the [211]-oriented Sb_2S_3 nanorods normally have the (001) planes tilting an angle of ca. 37° on substrate plane (Inset to Fig. 2d), it is revealed that the most competitive TiO_2 nanoparticle orientation for the heterogeneously epitaxial nucleation/growth of the [211]-oriented Sb_2S_3 single-crystalline nanorods features the tilting angle of $\alpha \approx 22^\circ$ (Supplementary Table 1, Supplementary Fig. 6 and Supplementary Note 5).

Actually, the intrinsic distinction between the growths of [211]-oriented Sb_2S_3 nanorods and [221]-oriented Sb_2S_3 cuboids originates from the sizes of [211]/[221]-oriented Sb_2S_3 seeds, that is, tiny Sb_2S_3 seeds of laterally < 10 nm in size for nanorods and large seeds of laterally 60–400 nm in size for cuboids (Supplementary Fig. 5 and Supplementary Note 4). Since the orientation and morphology of resulting Sb_2S_3 nanorods are exclusively governed by the tiny size of [211]/[221]-oriented Sb_2S_3 seeds (Supplementary Figs. 2–5 and Supplementary Notes 1–4), we here propose a tiny-seed-governed OCE nucleation/growth mechanism for the growth of [211]-oriented Sb_2S_3 nanorods and consequently the nanorod array on polycrystalline TiO_2 nanoparticle film (Supplementary Table 1, Supplementary Fig. 6

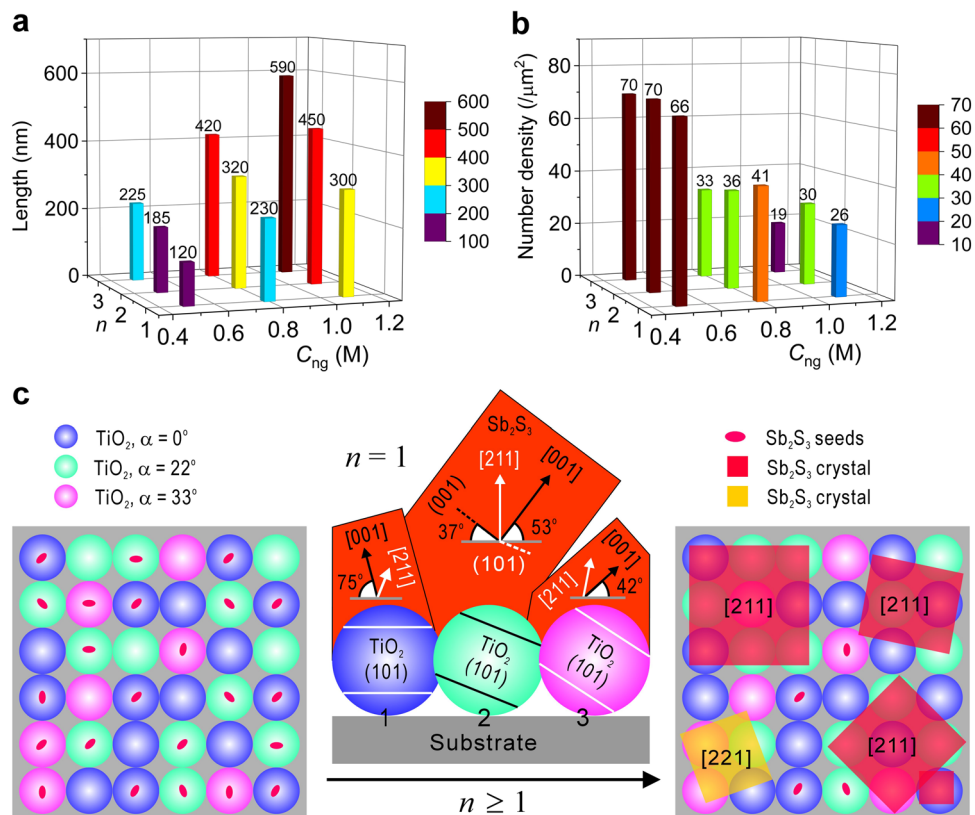


Fig. 3 Influencing factors and epitaxial growth model. **a** Length and **(b)** number density of Sb₂S₃ nanorods dependent on the nanorod growth solution concentration (C_{ng}) and the repetition of spin-coating and annealing (RSCA) cycle number (n) at the seed growth solution concentration of $C_{sg} = 0.1\text{ M}$. **c** Schematic illustration of the tiny-seed-governed orientation-competing-epitaxial nucleation/growth model for the growth of [211]-oriented Sb₂S₃ single-crystalline nanorods on polycrystalline TiO₂ nanoparticle film, where few other [221]-oriented ones, for example, might be possible. The inset to **c** shows the Sb₂S₃ crystal growth during the first RSCA cycle ($n = 1$), where the most competitive TiO₂ nanoparticle orientation for the Sb₂S₃ nanorod to nucleate/grow features its (101) plane tilting $\alpha = 22^\circ$ (Particle 2), but the nucleation/growth at other sites around (e.g., Particle 1 of $\alpha = 0^\circ$ and Particle 3 of $\alpha = 33^\circ$) is relatively much slower or suppressed due to their unfavorable TiO₂ (101) plane orientations for the [211]-oriented Sb₂S₃ crystal growth.

and Supplementary Note 5), as schematically illustrated in Fig. 3c. First, to form the [211]/[221]-oriented Sb₂S₃ seeds, the heterogeneously epitaxial nucleation of orthorhombic Sb₂S₃ crystals occurs on favorably oriented anatase TiO₂ nanoparticles, followed by the self-nucleated growth of the Sb₂S₃ nuclei into the Sb₂S₃ tiny crystalline seeds when the orientations of the Sb₂S₃ nuclei and the resulting seeds are governed by TiO₂ (101) plane orientations. Since the TiO₂ nanoparticles are relatively much larger (10–20 nm in diameter), each of the tiny Sb₂S₃ seeds (laterally <10 nm in size) has a high possibility to be formed on an individual TiO₂ nanoparticle. Those tiny Sb₂S₃ seeds inevitably have more chances to nucleate [211]-oriented Sb₂S₃ crystals, because more TiO₂ nanoparticles tending to orient with (101) face parallel to the film plane (Fig. 2d) inevitably result in more TiO₂ nanoparticle orientations in the range of $0^\circ \leq \alpha < 45^\circ$ (Supplementary Table 1, Supplementary Fig. 6 and Supplementary Note 5). During the first RSCA process (i.e., $n = 1$), the Sb₂S₃ seeds on the TiO₂ nanoparticles oriented with $\alpha \approx 22^\circ$ (Particle 2) have the fastest rate to take a self-nucleated growth into laterally enlarged Sb₂S₃ nanorods without changing the seed orientations, where the growth rate in c -axis direction is much larger than in a -axis and b -axis directions, but the Sb₂S₃ crystal growths at around sites with the less-competitive/unfavorable orientations (Particles 1 and 3) are merged or suppressed (Inset to Fig. 3c). Furthermore, with increasing the RSCA cycle numbers ($n > 1$), the growing nanorods still take a self-nucleated growth mainly along c -axis direction into longer ones without remarkably increasing lateral size (Supplementary Fig. 4 and Supplementary Note 3) nor

changing the orientation (Supplementary Fig. 7). During the nanorod growth, the sites, where there are no seeds and/or suppressed/merged crystal growths, create the empty interspaces in between nanorods, leading to the array of [211]-oriented Sb₂S₃ nanorods on the polycrystalline TiO₂ nanoparticle film. On the other hand, the tiny Sb₂S₃ seeds have a weak capability to merge and suppress the far-off nucleation at around sites due to their small size, leading to the number density (ca. $36\ \mu\text{m}^{-2}$) of Sb₂S₃ nanorods much higher than that (ca. $3\ \mu\text{m}^{-2}$) of the Sb₂S₃ cuboids derived from large Sb₂S₃ seeds (Supplementary Figs. 3, 5 and Supplementary Notes 2, 4).

Solar cell architecture and working principle. The Sb₂S₃ nanorod array in the Sb₂S₃/TiO₂-NHJ shows an absorption onset at about 737 nm corresponding to the optical band gap (E_g) of 1.68 eV (Fig. 4a), very close to the E_g value of Sb₂S₃ bulk crystal²⁵. With the valence band level (E_{VB}) of $E_{VB} = -5.29\ \text{eV}$ for the Sb₂S₃ bulk crystals²⁵, the conduction band level (E_{CB}) of the Sb₂S₃ nanorod array is calculated to be $-3.61\ \text{eV}$ from the E_g value; moreover, the PTB7-th exhibits the absorption mainly within 550–750 nm with an absorption onset at ca. 772 nm, corresponding to $E_g = 1.61\ \text{eV}$, the highest occupied molecular orbital (HOMO) energy level of $-5.20\ \text{eV}$ and the lowest unoccupied molecular orbital (LUMO) energy level of $-3.59\ \text{eV}$ ²⁶. With the $E_{CB} = -4.20\ \text{eV}$ for TiO₂²⁷, the $E_{CB} = -2.30\ \text{eV}$ and $E_{VB} = -5.30\ \text{eV}$ for MoO₃²⁸ and the work-functions (W_f) of $-4.40\ \text{eV}$ for FTO and $-5.10\ \text{eV}$ for Au²⁹, the combination of Sb₂S₃/TiO₂-NHJ and PTB7-th renders a ternary materials system, where TiO₂, Sb₂S₃

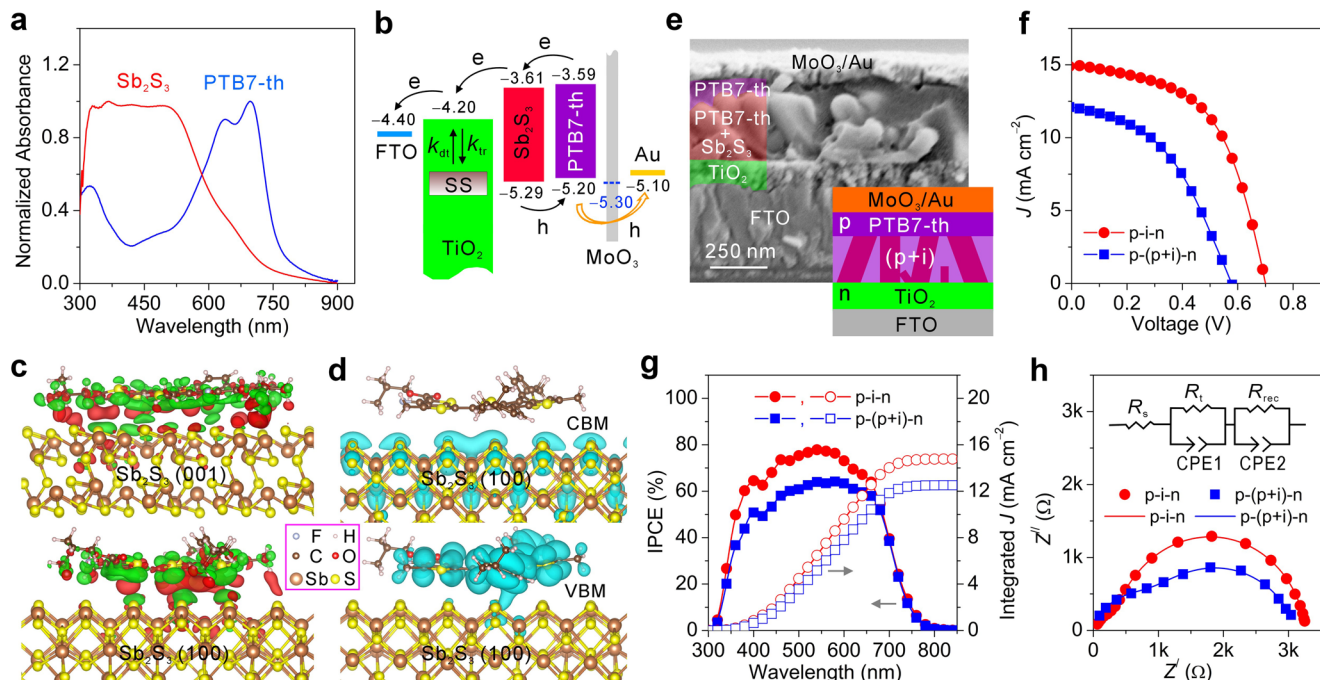


Fig. 4 Material property and architecture-dependent device performance. **a** Absorption spectra of $\text{Sb}_2\text{S}_3/\text{TiO}_2$ -nanoarray heterojunction ($\text{Sb}_2\text{S}_3/\text{TiO}_2$ -NHJ) and PTB7-th film. **b** Energy level diagram and charge transfers amongst the materials in the solar cells of this work, where the photogenerated electrons injected into the conduction band of TiO_2 may be trapped (k_{tr}) by surface states (SS) and the trapped electrons can be thermally released (k_{tr}) into the conduction band for transport. **c** Density functional theory (DFT) calculated interfacial interaction at the $\text{Sb}_2\text{S}_3/\text{PTB7-th}$ interfaces formed by PTB7-th on Sb_2S_3 (001) plane (above) and Sb_2S_3 (100) plan (below), where red color denotes charge accumulation and green color stands for charge depletion, and the electron density isosurface is set to $0.0004 \text{ e} \text{ \AA}^{-3}$. **d** DFT calculated wavefunctions of electronic states near the conduction band minimum (CBM) (above) and valence band maximum (VBM) (below) of $\text{Sb}_2\text{S}_3(100)/\text{PTB7-th}$ interface system, where the isosurface of wavefunction square is set to $4 \times 10^{-11} \text{ e} \text{ \AA}^{-3}$. **e** Structure of p-(p+i)-n solar cell (up-left: cross-sectional scanning electron microscopy image of a practical device; below-right: schematic illustration), where p means p-type PTB7-th, i means intrinsic Sb_2S_3 and n means n-type TiO_2 . **f** Current-voltage curves under AM1.5 G illumination, **(g)** incident photon-to-current conversion efficiency (IPCE) spectra (the right-hand axis shows the integrated photocurrent from the IPCE spectra) and **(h)** electrochemical impedance spectroscopic spectra (scatter: experimental data measured in the dark; solid line: fitting data) of the p-i-n and p-(p+i)-n solar cells with the highest efficiency. Inset to **(h)** shows the equivalent circuit used for fitting, which consists of series resistance (R_s), a hole transport and extraction resistance (R_t) at selective electrode, a recombination resistance (R_{rec}), and two constant phase angle elements (CPE).

and PTB7-th components form type II hybrid heterojunctions with staggered band alignments to facilitate the charge transport in solar cell (Fig. 4b). The Sb_2S_3 nanorod has a faceted top of (001) plane and the faceted sides of (100) and (010) planes (Fig. 2c). Density functional theory (DFT) calculations reveal that the S atoms of PTB7-th interact weakly with the Sb atoms on Sb_2S_3 (001) and (100) planes, but no evident interfacial electric field is formed at the $\text{Sb}_2\text{S}_3/\text{PTB7-th}$ interfaces (Fig. 4c); moreover, the $\text{Sb}_2\text{S}_3/\text{PTB7-th}$ interfaces formed by other Sb_2S_3 planes (e.g., (010) and (110) ones) have the same interfacial interaction features (Supplementary Fig. 8). The wavefunctions of electronic states near the conduction band minimum (CBM) and valence band maximum (VBM) of the $\text{Sb}_2\text{S}_3/\text{PTB7-th}$ interfaces formed by Sb_2S_3 (100) plane (Fig. 4d), and Sb_2S_3 (001), (010), and (110) planes as well (Supplementary Fig. 8), are also calculated using DFT. It is found that the CBM wavefunction only locates in the Sb_2S_3 material, but the VBM wavefunction predominantly distributes within the PTB7-th phase and slightly overlaps the Sb_2S_3 material, which is similar to the well-known efficient poly(3-hexylthiophene)/[6,6]-phenyl-C61-butyric acid methyl ester (i.e., P3HT/PCBM) organic photovoltaic system³⁰. Those unique separate electronic states inevitably favor the dissociation and injection of photogenerated electron-hole pairs and free charge carriers at the $\text{Sb}_2\text{S}_3/\text{PTB7-th}$ interface upon the excitation of Sb_2S_3 and PTB7-th, with the photogenerated electrons remaining

in or being injected into Sb_2S_3 crystal and the photogenerated holes being injected into or remaining in PTB7-th phase.

The p-i-n solar cells (Fig. 1) are fabricated by spin-coating PTB7-th onto the $\text{Sb}_2\text{S}_3/\text{TiO}_2$ -NHJ. Optimizing experiments demonstrate that the p-i-n solar cell delivers a peak efficiency when the $\text{Sb}_2\text{S}_3/\text{TiO}_2$ -NHJ is derived either at $C_{sg} = 0.1 \text{ M}$ (Supplementary Table 2) or at $C_{ng} = 0.8 \text{ M}$ and $n = 2$ (Supplementary Table 3). In the following sections, therefore, we focus on the optimized $\text{Sb}_2\text{S}_3/\text{TiO}_2$ -NHJ with a length of 320 nm prepared at $C_{sg} = 0.1 \text{ M}$, $C_{ng} = 0.8 \text{ M}$, and $n = 2$, to investigate the architecture-dependent performance of solar cells. In order to reveal the photovoltaic characteristics of the p-i-n architecture, we also fabricate the p-(p+i)-n counterpart solar cells for comparison, which features the polymer infiltration into the interspaces between nanorods resulting in the (p+i) blend of intrinsic Sb_2S_3 nanorods and p-type polymer sandwiched between p-type HTL and n-type ETL (Fig. 4e). To further visualize the PTB7-th infiltration into the Sb_2S_3 nanorod array, the SEM image with a larger view field is shown in Supplementary Fig. 9. As illustrated by Fig. 4b, in both p-i-n and p-(p+i)-n devices, free charge carriers are generated in the Sb_2S_3 nanorods upon illumination as the result of the small exciton binding energy (E_b) in Sb_2S_3 ($E_b < 10 \text{ meV}$) that is much smaller than the thermal energy at ambient temperature ($k_B T \sim 26 \text{ meV}$, where k_B is Boltzmann constant and T is temperature)³¹; however, the excitons generated in the PTB7-th phase upon

illumination need to diffuse to the $\text{Sb}_2\text{S}_3/\text{PTB7-th}$ interface for dissociation into free electrons (e) and holes (h), with the electrons being injected into Sb_2S_3 and the holes remaining in the polymer, because the E_b in conjugated polymers is normally about 0.4–0.5 eV^{32,33}, much higher than $k_B T \sim 26$ meV. Due to the high electron ($\mu_e \approx 10$ cm² V⁻¹ s⁻¹) and hole ($\mu_h \approx 2.6$ cm² V⁻¹ s⁻¹) mobilities in the Sb_2S_3 crystals¹⁹, the electrons generated in the Sb_2S_3 nanorods are quickly transported into the TiO_2 layer under the built-in electric field (E_{bi}) due to the W_f difference between the FTO and Au asymmetric collection electrodes^{34,35}, while the holes generated in the Sb_2S_3 nanorods are injected into the PTB7-th layer on nanorod top in the p-i-n device or the PTB7-th layers on nanorod top and amongst nanorods in the p-(p+i)-n device. As the result of quite a low hole mobility in the PTB7-th ($\mu_h = 2.8 \times 10^{-4}$ cm² V⁻¹ s⁻¹)³⁶, the transport of holes in the polymer phase proceeds very slowly and they finally tunnel through the MoO_3 layer acting as an optical spacer/Au diffusion barrier³⁷ to reach the Au electrode (Fig. 4b).

Architecture-dependent photovoltaic performance. The current-voltage ($J-V$) curves for the best p-i-n and p-(p+i)-n solar cells are presented in Fig. 4f, and the averaged performance of seven independent devices for each sample are summarized in Table 1. We achieve a champion efficiency of $\eta = 5.70\%$ in the p-i-n solar cells, which is comparable to those of the planar heterojunction solar cells based on the Sb_2S_3 nanoparticle films prepared by atomic layer deposition (e.g., $\eta = 5.77\%$)¹⁵ and solution-processing method (e.g., $\eta = 5.69\%$)¹⁷. Furthermore, the p-i-n solar cell exhibits good stability and retains 88% of the initial efficiency after storage in the N_2 atmosphere for 31 days (Supplementary Fig. 10). Generally, the p-i-n solar cells are much more efficient than the p-(p+i)-n ones. The averaged fill factor (FF) of the p-i-n devices is ca. 54%, much higher than that (ca. 38%) of the p-(p+i)-n ones, and the increased FF in the p-i-n devices is accompanied by a larger open-circuit voltage (V_{oc}), a higher short-circuit current (J_{sc}), a smaller series resistance (R_s), and a larger shunt resistance (R_{sh}) (Table 1). Moreover, incident photon-to-current conversion efficiency (IPCE) spectra show that both p-i-n and p-(p+i)-n solar cells have a similar and broad spectral profile in 300–750 nm, and the integrated J_{sc} from the IPCE data (i.e., 14.78 mA cm⁻² for p-i-n device and 12.51 mA cm⁻² for p-(p+i)-n one) agree with the observed J_{sc} values (Fig. 4g). While the polymer amount accumulated in the p-(p+i)-n architecture is higher than that in the p-i-n one, the IPCE of the former device in the whole absorption range is significantly lower than that of the latter one, inferring that much more photogenerated charge carriers contribute to photocurrent generation in the p-i-n device.

The electrochemical impedance spectroscopy (EIS) spectra in the form of Nyquist plots for the p-i-n and p-(p+i)-n solar cells measured in the dark are shown in Fig. 4h. The EIS data are fitted with a transmission line model³⁸ as depicted by a simplified equivalent circuit (Inset to Fig. 4f), and the fitting results are summarized in Supplementary Table 4. On the Nyquist plots, the small arc at high frequency is for the hole transport and extraction resistance (R_t) at the selective electrode, while the main arc at low frequency is attributed to recombination resistance (R_{rec}) in the devices³⁹. The p-i-n solar cell has $R_t = 32.08$ Ω cm², much smaller than that ($R_t = 74.58$ Ω cm²) of the p-(p+i)-n device, inferring that the p-i-n architecture has a much easier hole the transport and extraction at the MoO_3/Au cathode. Moreover, the R_{rec} value (204.66 Ω cm²) in the p-(p+i)-n device is lower than that (260.10 Ω cm²) in the p-i-n one, suggesting much more serious charge recombination in the p-(p+i)-n device. Furthermore, the series resistance (R_s) in the p-(p+i)-n

Table 1 Architecture-dependent photovoltaic performance of the p-i-n and p-(p+i)-n solar cells^a.

Device	V_{oc} (V)	J_{sc} (mA cm ⁻²)	FF (%)	η (%)	R_s (Ω cm ²)	R_{sh} (Ω cm ²)	τ_{e1} (ms)	τ_{e2} (μ s)	τ_D (μ s)
p-i-n	0.69 ± 0.01	14.20 ± 0.79	54.44 ± 1.10	5.36 ± 0.22	11.34 ± 0.70	361.61 ± 55.85	818.39 ± 172.29	51.23 ± 5.58	7.06 ± 0.93 ^b
p-(p+i)-n	0.70	14.98	54.60	5.70	10.54	361.98	895.44	61.22	6.25 ^c
	0.58 ± 0.01	11.49 ± 0.36	38.46 ± 3.52	2.58 ± 0.32	30.24 ± 6.32	225.93 ± 26.03	66.36 ± 31.80	37.41 ± 7.41	19.56 ± 0.01 ^b
	0.58	12.06	44.18	3.08	21.62	264.55	31.53	38.74	19.55 ^c

^aThe Sb_2S_3 nanorod arrays are 320 nm in length and prepared at the seed growth solution concentration of $C_{se} = 0.1$ M, the nanorod growth solution concentration of $C_{ng} = 0.8$ M, and the repetition of spin-coating and annealing cycle number of $n = 2$; parameters V_{oc} , J_{sc} , FF, η , R_s , and R_{sh} stand, respectively, for the open-circuit voltage, short-circuit current, fill factor, power conversion efficiency, series resistance and shunt resistance obtained in the current-voltage measurements of solar cells; the lifetime (τ_e) and transit time (τ_D) of photogenerated electrons are measured with dynamic spectroscopies.

^bThe averaged data with standard deviations as errors are the statistic results of seven individual devices.

^cThe data for the device with the highest efficiency.

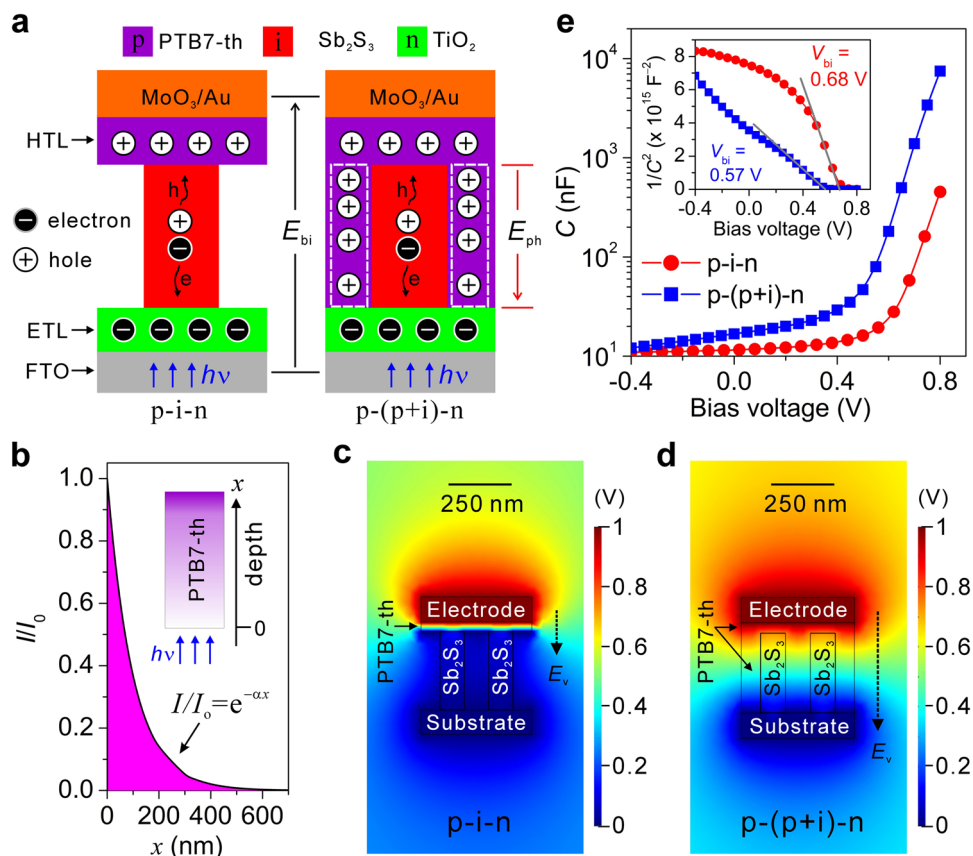


Fig. 5 Architecture-related photogenerated electric field effects. **a** Architecture-dependent charge distribution model showing the absence and presence of photogenerated electric field (E_{ph}) effects in the p-i-n (left) and p-(p+i)-n (right) solar cells during the photovoltaic process, where p means p-type PTB7-th to form hole transporting layer (HTL), i means intrinsic Sb_2S_3 and n means n-type TiO_2 to form electron transporting layer (ETL). **b** Light attenuation in the polymer film, where the inset illustrates the distribution of photogenerated excitons in the PTB7-th film along the illumination depth direction with a deeper purple for a smaller exciton population. **c, d** Simulated electric potential distributions in **(c)** p-i-n and **(d)** p-(p+i)-n solar cells at 1 V forward bias, where, E_v stands for the bias electrostatic field, the color gradient bars depict the electric potential, and the substrate and electrode refer to the FTO/ TiO_2 and MoO_3/Au layers in solar cells, respectively. **e** The capacitance-voltage data in the dark for the p-i-n and p-(p+i)-n solar cells with the highest efficiency.

device ($4.42 \Omega \text{ cm}^2$) is also much higher than that ($1.73 \Omega \text{ cm}^2$) in the p-i-n device, in agreement with the change in the R_s data measured by J - V characterization (Table 1).

Photogenerated electric field effects on photovoltaic performance. Obviously, the p-i-n and p-(p+i)-n hybrid solar cells exhibit a significantly architecture-dependent performance. A similar phenomenon has also been observed in the hybrid solar cells based on CdS nanorod array and conjugated polymer MEH-PPV, that is, a partial infiltration of MEH-PPV into CdS nanorod array results in better device performance, but for which the reason is not clear yet⁴⁰. Since materials in the p-i-n and p-(p+i)-n solar cells are the same, the observed different photovoltaic performances of them, in particular, the change in V_{oc} , must be governed by an architecture-dependent factor other than the materials property (e.g., band energy level difference).

Here, an architecture-dependent charge distribution (ADCD) model is proposed on the basis of light intensity attenuation in the polymer phase to describe the photovoltaic behaviors in the p-i-n and p-(p+i)-n devices, as schematically illustrated in Fig. 5a. In the p-(p+i)-n solar cells, the polymer phase in between the interspaces of Sb_2S_3 nanorods in the Sb_2S_3/TiO_2 -NHJ has a thickness comparable to the Sb_2S_3 nanorod length (i.e., 320 nm) and a remarkable absorption contribution to the generation of

charge carriers. Actually, the light intensity (I) is exponentially attenuated when passing a polymer film according to the relation of $I = I_0 \exp(-\alpha x)$, where I_0 is the incident light intensity, I is the intensity at the illumination depth of x nm and α is the absorption coefficient of PTB7-th. Given $\alpha = 10^5 \text{ cm}^{-1}$ for PTB7-th, the illumination intensity at the illumination depth of 320 nm is attenuated to 4% of the incident intensity (Fig. 5b). As the result of the light intensity attenuation, therefore, in the p-(p+i)-n solar cells, there is an original photogenerated hole density gradient from a higher density at the stem region of Sb_2S_3 nanorods to a lower one at the nanorod top region, after the photogenerated excitons in PTB7-th phase dissociate at the nanorod-side-face-formed $Sb_2S_3/PTB7$ -th interface with electrons being injected into the Sb_2S_3 nanorods. However, the conductivity of a conjugated polymer in pristine form is very low, but it increases under the photo-doped state due to illumination. Hence, subjected to the light intensity attenuation, the conductivity in the PTB7-th film inevitably becomes gradually reduced along the illumination depth direction. Consequently, during the photovoltaic process, with the diffusion of the photogenerated holes in between the interspaces amongst the Sb_2S_3 nanorods towards the MoO_3/Au collection electrode, a reversed hole density gradient is formed from a higher hole density at the nanorod top region to a lower one at the Sb_2S_3 nanorod stem region, to render a photogenerated electric field (E_{ph}) opposite to the E_{bi} in p-(p+i)-n architecture (right, Fig. 5a).

In contrast, the p-i-n solar cells are actually an E_{ph} -free device (left, Fig. 5a), due to the absence of the polymer infiltration into the interspaces in between the Sb_2S_3 nanorods and thereby no photogenerated hole accumulation around each of Sb_2S_3 nanorods.

We performed the finite element simulation of the bias electrostatic field (E_v) distribution in the p-i-n and p-(i+p)-n solar cells at a forward bias of 1 V, to mimic the case of selectively accumulated charge carriers in the devices, using the AC/DC module on commercial COMSOL Multiphysics software. The structural models for simulation (Supplementary Table 5) were built by assuming that all the nanorods of a right square prism shape are vertically grown on the substrate and the materials dimensions are given by referring to the SEM results (Figs. 1 and 4e). All the parameters of materials property and dimensions for simulation are provided in Supplementary Table 5. In the p-i-n solar cell, where the FTO/TiO₂ and MoO₃/Au layers are defined, respectively, as substrate and electrode for a simplified simulation, the highest electrostatic potential dominantly at the electrode gets gradually reduced along normal of HTL (i.e., PTB7-th film) until the lowest potential at the top of Sb_2S_3 nanorods, suggesting the presence of a very narrow bias E_v due to the forward bias in the HTL to drive electrons to move towards the electrode (Fig. 5c). As for the p-(p+i)-n solar cell, however, the highest electrostatic potential at the electrode gradually decreases along the axis of Sb_2S_3 nanorods until the lowest potential at the substrate, informing a bias E_v across the whole device to drive electrons to reach the electrode (Fig. 5d). Clearly, the simulations inform that, as the results of the hole accumulation near the nanorod top region and the electron accumulation in the nanorod stem region, an electric field (e.g., E_v) across the whole device and opposite to the built-in field E_{bi} is theoretically expected to reduce the collection efficiency of electrons photogenerated inside both Sb_2S_3 nanorods and PTB7-th phase in the p-(p+i)-n solar cells, while only an electric field across the HTL negatively affects the very limited population of electrons at the top of Sb_2S_3 nanorods and in the HTL in the p-i-n devices. The finite element simulations theoretically agree with the expectations from the ADCD model (Fig. 5a). Interestingly, further simulated results inform that once the PTB7-th infiltration into the Sb_2S_3 nanorod array is present either partially or completely, a similar electric field (e.g., E_v) distribution across the whole device and opposite to the built-in field E_{bi} is theoretically expected (Supplementary Fig. 11 and Supplementary Note 6).

The ADCD model in Fig. 5a is also experimentally supported by the capacitance-voltage ($C-V$) measurements of solar cells in the dark. The $C-V$ results (Fig. 5e) clearly show that the p-(i+p)-n device has a much higher capacitance (C) than the p-i-n one in the whole bias voltage (V) range, indicating a higher capability of being charged by injected charge carriers in the former device. The relation $C^{-2} \propto V$ in Mott-Schottky (MS) equation expresses the relationship amongst the C , built-in potential (V_{bi}), and V of the solar cell, and the intersection point of the linear slope with voltage axis on the $C^{-2}-V$ plot stands for the V_{bi} across the device^{41,42}. The V_{bi} of the p-i-n device is 0.68 V (Inset to Fig. 5e), comparable to the maximum theoretical V_{bi} (0.70 eV) in the solar cell due to the W_f difference between Au (-5.10 eV) and FTO (-4.40 eV) electrodes²⁹. Reasonably, the V_{bi} obtained from the $C^{-2}-V$ plots originates from the W_f offset of the asymmetric electrodes⁴³. However, the p-(p+i)-n device exhibits a V_{bi} of 0.57 V, much lower than the maximum theoretical V_{bi} value. The V_{bi} values of the p-i-n and p-(p+i)-n devices are almost identical to their V_{oc} data from $J-V$ measurements (Table 1).

The smaller V_{bi} accompanied by a higher capacitance at $V < V_{bi}$ in the p-(i+p)-n cell suggests that a negative impact on the V_{bi} results from the charge accumulation therein^{44,45}. Since there is a

greatly unbalance amongst the hole mobility in PTB7-th phase ($\mu_h = 2.8 \times 10^{-4} \text{ cm}^2 \text{ V}^{-1} \text{ s}^{-1}$) and the electron mobilities in TiO₂ ($\mu_e \approx 1.98 \times 10^{-3} \text{ cm}^2 \text{ V}^{-1} \text{ s}^{-1}$)²⁵ and Sb_2S_3 ($\mu_e \approx 10 \text{ cm}^2 \text{ V}^{-1} \text{ s}^{-1}$), the charge accumulation predominantly correlates with the low-mobility holes in the polymer phase in between Sb_2S_3 nanorods under forwarding bias⁴⁶, resulting in a distribution state of a high hole density toward the MoO₃/Au cathode and a high electron density in the TiO₂ layer. Clearly, the $C-V$ measurements reveal that an opposite electric field opposite to the E_{bi} across the device is generated due to the hole accumulation in the polymer phase in between the Sb_2S_3 nanorods with a distribution of a high density toward the MoO₃/Au cathode to impose a significant negative impact on the device V_{oc} in the p-(i+p)-n solar cells, but it is not the case in the p-i-n devices, in agreement with the expectations from the ADCD model.

Both the finite element simulation and $C-V$ data demonstrate that the E_{ph} negative effect on charge transport is much more noteworthy in p-(p+i)-n devices than in p-i-n ones. From the ADCD model (Fig. 5a), the following points can be expected: (i) the p-i-n device only have nanorod-top-face-formed Sb_2S_3 /PTB7-th interface, but the p-(p+i)-n device has additionally a much larger area of nanorod-side-face-formed Sb_2S_3 /PTB7-th interface besides the nanorod-top-face-formed one and a heavy photogenerated hole accumulation around each of nanorods, hence, the p-(p+i)-n device should have a much shorter electron lifetime (τ_{e1}) due to the charge recombination at the Sb_2S_3 /PTB7-th interface; (ii) as the TiO₂/ Sb_2S_3 interface in the p-i-n and p-(p+i)-n solar cells are the same, the electron lifetime (τ_{e2}) subjected to the charge recombination at TiO₂/ Sb_2S_3 interface in two solar cells should be comparable to each other, but, a more serious charge recombination at the TiO₂/ Sb_2S_3 interface for a shorter τ_{e2} should practically exist in the p-(p+i)-n device because the photogenerated holes in Sb_2S_3 nanorods do not easily escape from the TiO₂/ Sb_2S_3 interface under the E_{ph} effect; (iii) the transit time (τ_D) for the photogenerated electrons accommodating in the TiO₂ layer to reach the FTO collection electrode in the p-(p+i)-n device should be much longer than that in the p-i-n one, because the electron diffusion rate greatly depends on the electron concentration in conduction band⁴⁷, and the electron density injected into the TiO₂ layer in the p-(p+i)-n device is much lower due to the serious loss by interfacial charge recombination at nanorod-side-face-formed Sb_2S_3 /PTB7-th interface. Those expectations are confirmed by dynamic spectroscopic investigations of solar cells (Supplementary Fig. 12 and Supplementary Note 7). That is, the $\tau_{e1} = 31.53 \text{ ms}$ of the p-(p+i)-n device is much shorter than the $\tau_{e1} = 895.44 \text{ ms}$ in the p-i-n device; both cells have comparable τ_{e2} values, but the $\tau_{e2} = 38.74 \text{ }\mu\text{s}$ for p-(p+i)-n cell is shorter than the $\tau_{e2} = 61.22 \text{ }\mu\text{s}$ for p-i-n cell; moreover, the $\tau_D = 19.55 \text{ }\mu\text{s}$ in p-(p+i)-n device is much longer than $\tau_D = 6.25 \text{ }\mu\text{s}$ in the p-i-n device (Table 1). Surprisingly, the p-i-n device has a very long electron lifetime τ_{e1} related to the charge recombination at Sb_2S_3 /PTB7-th interface, which is attributed to a very low electron population at the top of Sb_2S_3 nanorods in such device as the result of the high electron transport in the Sb_2S_3 nanorods toward FTO collection electrode. Moreover, the very low electron population in the Sb_2S_3 nanorod top region inevitably results in a limited negative impact of the E_{ph} across the HTL on the transport of photogenerated electrons in the p-i-n device, as indicated by the finite element simulation (Fig. 5c).

Advantages of the p-i-n solar cells. The observed $J-V$ characteristic difference between the p-i-n and p-(p+i)-n devices (Fig. 4f and Table 1) gets well accounted for by the proposed ADCD mode (Fig. 5a). First, after ruling out the band energy level influence on the device V_{oc} , it is reasonable to believe that the V_{oc}

of the $\text{Sb}_2\text{S}_3/\text{TiO}_2\text{-NHJ}$ solar cells strongly correlates with the net built-in field in device^{34,35}. Since the p-i-n solar cell under illumination has no negative E_{ph} effects as the result of lacking the photogenerated hole accumulation around Sb_2S_3 nanorods, the device has a higher V_{oc} resulting from the E_{bi} across the device due to the asymmetric W_f values between Au and FTO electrodes, while there are the negative E_{ph} effects to weaken the device E_{bi} under illumination for a reduced V_{oc} in the p-(i + p)-n device. Moreover, a larger nanorod-side-face-formed $\text{Sb}_2\text{S}_3/\text{PTB7-th}$ interface area and the negative E_{ph} effects on charge transport are existing in the p-(i + p)-n device, which deteriorate the charge collection efficiency to reduce reduced J_{sc} and FF by causing a great electrical coupling between the electrons inside Sb_2S_3 nanorods and the holes in PTB7-th phase with a small R_{sh} for serious interfacial charge recombination at the $\text{Sb}_2\text{S}_3/\text{PTB7-th}$ interface and a high R_s for a retarded charge transport.

Obviously, the p-i-n solar cells based on $\text{Sb}_2\text{S}_3/\text{TiO}_2\text{-NHJ}$ have at least two unique advantages: one is that no negative E_{ph} effects on device performance thanks to lacking the photogenerated hole accumulation around Sb_2S_3 nanorods; another is the [211]-oriented single-crystalline Sb_2S_3 nanorods therein provide the straightforward and highly effective charge transport channels formed by the covalently bounded $(\text{Sb}_4\text{S}_6)_n$ ribbons tilting ca. 53° on the substrate for the photogenerated charge carriers inside the Sb_2S_3 layer to reach collection electrode. Indeed, those advantages make the $\text{Sb}_2\text{S}_3/\text{TiO}_2\text{-NHJ}$ have a good application potential to efficient solar cells. However, while the efficiency ($\eta = 5.70\%$) of our p-i-n solar cells is comparable to the hybrid planar heterojunction solar cell based on the Sb_2S_3 nanoparticle film (i.e., FTO/ $\text{TiO}_2/\text{Sb}_2\text{S}_3/\text{P3HT}/\text{Au}$ ($\eta = 5.77\%$)¹⁵, but it is still much lower than those of all-inorganic solar cells of the Sb_2Se_3 nanorod array on Mo-substrate (i.e., Mo/MoSe₂/ $\text{Sb}_2\text{Se}_3/\text{CdS}/\text{ZnO}/\text{ZnO}:\text{Al}/\text{Ag}$, $\eta = 9.2\%$)²² and the InP p-n junction nanowire array on InP substrate (i.e., InP/InP(p-n)/ITO, $\eta = 17.8\%$)⁹. For a simple preparation of an HTL over the $\text{Sb}_2\text{S}_3/\text{TiO}_2\text{-NHJ}$ without infiltration into the interspaces in-between nanorods, we chose the good-performing polymer PTB7-th to prepare organic HTL. The not high efficiency in our p-i-n solar cells reasonably originates from the low hole mobility in PTB7-th and the weak interaction between the PTB7-th and Sb_2S_3 as indicated by DFT calculation (Fig. 4c) for a not very efficient $\text{Sb}_2\text{S}_3/\text{PTB7-th}$ interface for charge separation and injection⁴⁸. We envision that in order to get the more efficient p-i-n solar cells based on the $\text{Sb}_2\text{S}_3/\text{TiO}_2\text{-NHJ}$, it is necessary to replace the polymer HTL with one of high hole mobility, where the HTL material needs to be prevented from infiltrating into the interspaces in-between nanorods, for example, by planarizing the nanoarray with an insulating substance infiltrated into the interspaces among nanorods^{8,9,11}.

Discussion

In summary, the Sb_2S_3 nanorod array on polycrystalline TiO_2 film is realized by a tiny-seed-assisted RSCA method, offering a nanoarray heterojunction system (i.e., $\text{Sb}_2\text{S}_3/\text{TiO}_2\text{-NHJ}$) with the preferentially [211]-orientated Sb_2S_3 nanorods of lateral sizes much larger than the beneath TiO_2 nanoparticles. The Sb_2S_3 nanorods in the $\text{Sb}_2\text{S}_3/\text{TiO}_2\text{-NHJ}$ have a bandgap of $E_{\text{g}} = 1.68$ eV and provide straightforward and highly effective charge transport channels formed by covalently bounded $(\text{Sb}_4\text{S}_6)_n$ ribbons. Those make the $\text{Sb}_2\text{S}_3/\text{TiO}_2\text{-NHJ}$ have a good potential for efficient solar cells. By depositing a conjugated polymer PTB7-th film as a hole transporting layer onto the top of the $\text{Sb}_2\text{S}_3/\text{TiO}_2\text{-NHJ}$, a hybrid solar cell with a p-i-n architecture is obtained. The p-i-n solar cells exhibit a V_{oc} strongly correlating with the net built-in field across devices and no negative E_{ph} impact on device performance. With the two unique advantages of the straightforward and effective charge transport channels and the absence of negative

E_{ph} impact on device performance, a power conversion efficiency of 5.70% is achieved in the p-i-n solar cells for an optimized nanoarray structure (i.e., 320-nm-thick Sb_2S_3 nanoarray prepared at $C_{\text{sg}} = 0.1$ M, $C_{\text{ng}} = 0.8$ M and $n = 2$). Due to the absence of the negative E_{ph} impact, the p-i-n solar cells exhibit a long electron lifetime on the sub-second scale ($\tau_{\text{e1}} \approx 0.9$ s) related to the charge recombination at $\text{Sb}_2\text{S}_3/\text{PTB7-th}$ interface.

The orientation and morphology of the resulting Sb_2S_3 nanorods on the TiO_2 film are exclusively governed by the tiny [211]/[221]-oriented Sb_2S_3 seeds of laterally <10 nm in size. The growth of the [211]-oriented Sb_2S_3 nanorods follows a tiny-seed-governed OCE nucleation/growth mechanism according to the epitaxial relationship of Sb_2S_3 (101)// TiO_2 (101), where the Sb_2S_3 seeds on the TiO_2 nanoparticles oriented with $\alpha \approx 22^\circ$ are most competitive during the followed RSCA cycles ($n \geq 1$) to take a self-nucleated growth into much larger [211]-oriented Sb_2S_3 nanorods with a much larger growth rate in *c*-axis direction than in *a*-axis and *b*-axis directions. During the tiny-seed-governed OCE nucleation/growth process, the sites there are no seeds and/or suppressed/merged crystal growths create the empty interspaces in between nanorods for the formation of the Sb_2S_3 nanorod array. Moreover, the length of nanorods (i.e., nanoarray thickness) strongly depends on both C_{ng} and n values; the lateral size and the number density of the Sb_2S_3 nanorods are mainly obtained at the first RSCA cycle ($n = 1$) and not *n*-dependent, while they are affected by C_{ng} and increasing C_{ng} leads to increased lateral size and reduced number density.

In the $\text{Sb}_2\text{S}_3/\text{PTB7-th}$ hybrid system, no evident interfacial electric field is formed at the $\text{Sb}_2\text{S}_3/\text{PTB7-th}$ interfaces due to the weak interaction between the organic and inorganic components; however, the wavefunctions of electronic states near the CBM and VBM of the $\text{Sb}_2\text{S}_3/\text{PTB7-th}$ interface mainly locates in the Sb_2S_3 and PTB7-th phases, respectively, resulting in the unique separate electronic states favorable to the dissociation and injection of photogenerated electron-hole pairs and free charge carriers at the $\text{Sb}_2\text{S}_3/\text{PTB7-th}$ interface upon the excitation of Sb_2S_3 and PTB7-th, with the electrons remaining in or being injected into Sb_2S_3 crystal and the holes being injected into or remaining in PTB7-th phase. The solar cells with p-i-n architecture, consisting of $\text{Sb}_2\text{S}_3/\text{TiO}_2\text{-NHJ}$ and PTB7-th, exhibits no negative E_{ph} effects on device performance, which is well accounted for by the ADCD model proposed on the basis of light intensity attenuation in the polymer phase and verified by the finite element simulations and *C* - *V* measurements. In contrast, in the p-(p + i)-n counterpart solar cell, the negative E_{ph} effects mainly manifest themselves to reduce the opposite built-in field E_{bi} across the device, to retard the charge transport and to cause the serious recombination for a seriously deteriorated overall device performance (V_{oc} , J_{sc} , FF, and IPCE).

Our results provide a facile solution-processing method to prepare the high-quality $\text{Sb}_2\text{S}_3/\text{TiO}_2$ nanoarray heterojunction system with preferentially orientated, straightforward, and highly efficient charge transport channels for photovoltaic and other optoelectronic applications, as well as an understanding of the heterogeneously epitaxial growth of single-crystalline nanorods on the polycrystalline surface. Moreover, the NHJ material system and the p-i-n solar cell without the negative impact of E_{ph} on device performance offer the guides to the conceptual design of the efficient photoactive layer and device configuration in the solar cells based on nanorod/nanowire arrays, in particular, the devices configured using a partner material with a greatly unbalanced charge transport property.

Methods

Sb_2S_3 precursor solution. The Sb_2S_3 precursor solution was prepared by a method similar to our previous report except for the addition of glycerin¹⁹. Briefly,

0.8 mmol of SbCl_3 ($\geq 99.0\%$, Alfa Aesar) and 1.44 mmol of thiourea ($\geq 99.0\%$, Alfa Aesar) were sequentially dissolved in 1 ml of N,N -dimethylformamide (DMF) under stirring at room temperature, resulting in a clear yellow precursor solution with 0.8 M SbCl_3 and an SbCl_3 /thiourea molar ratio of 1:1.8, which is stable for weeks in ambient conditions. The different SG and NG solutions were derived from this precursor solution by DMF dilution. The concentrations of the SG (i.e., C_{sg}) and NG (i.e., C_{ng}) solutions were defined by the molecular concentration of SbCl_3 dissolved therein.

Preparation of $\text{Sb}_2\text{S}_3/\text{TiO}_2$ -NHJ. The FTO glass substrates ($25 \times 25 \text{ mm}^2$, ca. $14 \Omega \text{ sq}^{-1}$) patterned into stripes ($20 \times 4 \text{ mm}^2$) in the middle part of the substrate by laser were commercially obtained from the Advanced Election Technology Co. Ltd., Liaoning Province, China. The FTO substrates were ultrasonically cleaned with acetone, isopropanol, and deionized water for 20 min, respectively, and then further cleaned with UV-Ozone for 15 min and washed with ethanol before use. A compact and polycrystalline TiO_2 nanoparticle film of ca. 110 nm in thickness was prepared on the FTO substrate as described elsewhere¹⁹.

$\text{Sb}_2\text{S}_3/\text{TiO}_2$ -NHJ was prepared by a tiny-seed assisted RSCA method. Typically, the Sb_2S_3 precursor deposited onto the TiO_2 film by spin-coating (3000 rpm, 40 s) the SG solution (120 μl ; normally $C_{\text{sg}} = 0.1 \text{ M}$, unless otherwise specified) was sequentially annealed at 150°C for 5 min and 300°C for 10 min on a hotplate in an N_2 -protected glovebox, resulting in tiny Sb_2S_3 seeds on the TiO_2 film. A transparent Sb_2S_3 precursor film was prepared on a tiny Sb_2S_3 seeds-decorated TiO_2 film by spin-coating (3000 rpm, 40 s) the NG solution (120 μl ; normally $C_{\text{ng}} = 0.8 \text{ M}$, unless otherwise specified) and thermally annealed by the route identical with that for the Sb_2S_3 seed formation, which was referred to as one RSCA cycle. After the seed-decorated TiO_2 film had been subjected to several RSCA cycle numbers (n), the $\text{Sb}_2\text{S}_3/\text{TiO}_2$ -NHJ with a desirable length was in situ formed on the FTO substrate.

Solar cell fabrication. PTB7-th ($M_w \sim 180,000$; $M_w/M_n \sim 2.5$, 1-Material) was dissolved in chlorobenzene and stirred overnight at 60°C ; after the solution was naturally cooled down to room temperature, the PTB7-th solution (15 mg ml^{-1}) for spin-coating was obtained. To prepare p-i-n solar cells (Fig. 1), a PTB7-th film was spin-coated (2000 rpm, 60 s) onto the top of the $\text{Sb}_2\text{S}_3/\text{TiO}_2$ -NHJ from the PTB7-th solution (70 μl) and annealed at 100°C for 15 min to eliminate the solvent residue, where the spin-coating was immediately carried out once the PTB7-th solution was loaded. In order to prepare p-(p+i)-n solar cells (Fig. 4e), the PTB7-th solution droplet (70 μl) was first loaded onto the $\text{Sb}_2\text{S}_3/\text{TiO}_2$ -NHJ and kept in the chlorobenzene atmosphere overnight for the infiltration of the polymer into the interspaces amongst the Sb_2S_3 nanorods; then, the sample was dried by rotating (2000 rpm, 60 s) and further annealed at 100°C for 15 min to remove the solvent. Finally, an 8-nm-thick molybdenum oxide (MoO_3) film and a 100-nm-thick gold electrode were sequentially evaporated onto the PTB7-th layer under a pressure of $5.0 \times 10^{-4} \text{ Pa}$. The optimized Sb_2S_3 nanorod array for efficient solar cells was prepared at $C_{\text{sg}} = 0.1 \text{ M}$, $C_{\text{ng}} = 0.8 \text{ M}$ and $n = 2$.

Sample characterization and DFT calculation. The J - V curves of solar cells were measured with forwarding scan and dwell time of 50 s on a 94023 A Oriol[®]Sol3A solar simulator (Newport, Inc.) under AM 1.5 G illumination (100 mW cm^{-2}) at room temperature in air, and the light intensity from a 450 W xenon lamp was calibrated with a standard crystalline silicon solar cell. The J - V curves were collected with an Oriol[®] I-V test station (PVIV-1A, Keithley 2400 Source Meter, Labview 2009 SP1 GUI Software, Newport, Inc.). During the J - V measurements, the illumination area was limited by a mask with an aperture ($3 \times 3 \text{ mm}^2$), which actually defined the effective area for getting the photovoltaic parameters of the device. The characterizations of film samples, other characterizations of solar cells, and the DFT calculation method are provided in Supplementary Methods.

Reporting summary. Further information on research design is available in the Nature Research Reporting Summary linked to this article.

Data availability

The authors declare that the data supporting the findings of this study are available within the paper and its Supplementary Information files. Extra data are available from the corresponding author (M.W.) upon reasonable request.

Received: 22 December 2020; Accepted: 16 July 2021;

Published online: 05 August 2021

References

- Garnett, E. & Yang, P. Light trapping in silicon nanowire solar cells. *Nano Lett.* **10**, 1082–1087 (2010).

- Yu, P. et al. Design and fabrication of silicon nanowires towards efficient solar cells. *Nano Today* **11**, 704–737 (2016).
- Kelzenberg, M. D. et al. Enhanced absorption and carrier collection in Si wire arrays for photovoltaic applications. *Nat. Mater.* **9**, 239–244 (2010).
- Krogstrup, P. et al. Single-nanowire solar cells beyond the Shockley–Queisser limit. *Nat. Photon.* **7**, 306–310 (2013).
- Otnes, G. & Borgström, M. T. Towards high efficiency nanowire solar cells. *Nano Today* **12**, 31–45 (2017).
- Goktas, N. I. et al. Nanowires for energy: a review. *Appl. Phys. Rev.* **5**, 041305 (2018).
- Li, Z., Tan, H. H., Jagadish, C. & Fu, L. III–V semiconductor single nanowire solar cells: a review. *Adv. Mater. Technol.* **3**, 1800005 (2018).
- Cui, Y. et al. Efficiency enhancement of InP nanowire solar cells by surface cleaning. *Nano Lett.* **13**, 4113–4117 (2013).
- van Dam, D. et al. High-efficiency nanowire solar cells with omnidirectionally enhanced absorption due to self-aligned indium-tin-oxide mie scatterers. *ACS Nano* **10**, 11414–11419 (2016).
- Wallentin, J. et al. InP nanowire array solar cells achieving 13.8% efficiency by exceeding the ray optics limit. *Science* **339**, 1057–1060 (2013).
- Yao, M. et al. GaAs nanowire array solar cells with axial p-i-n junctions. *Nano Lett.* **14**, 3293–3303 (2014).
- Kondrotas, R., Chen, C. & Tang, J. Sb_2S_3 solar cells. *Joule* **2**, 857–878 (2018).
- Rühle, S. Tabulated values of the Shockley–Queisser limit for single junction solar cells. *Sol. Energy* **130**, 139–147 (2016).
- Choi, Y. C., Lee, D. U., Noh, J. H., Kim, E. K. & Seok, S. I. Highly improved Sb_2S_3 sensitized-inorganic-organic heterojunction solar cells and quantification of traps by deep-level transient spectroscopy. *Adv. Funct. Mater.* **24**, 3587–3592 (2014).
- Kim, D.-H. et al. Highly reproducible planar Sb_2S_3 -sensitized solar cells based on atomic layer deposition. *Nanoscale* **6**, 14549–14554 (2014).
- Tang, R. et al. Vacuum assisted solution processing for highly efficient Sb_2S_3 solar cells. *J. Mater. Chem. A* **6**, 16322–16327 (2018).
- Zhang, L. et al. Sequential deposition route to efficient Sb_2S_3 solar cells. *J. Mater. Chem. A* **6**, 21320–21326 (2018).
- Yuan, S. et al. Efficient planar antimony sulfide thin film photovoltaics with large grain and preferential growth. *Sol. Energy Mater. Sol. Cells* **157**, 887–893 (2016).
- Chen, J. et al. Preferentially oriented large antimony trisulfide single-crystalline cuboids grown on polycrystalline titania film for solar cells. *Commun. Chem.* **2**, 121 (2019).
- Zhong, M. et al. High-performance photodetectors based on Sb_2S_3 nanowires: wavelength dependence and wide temperature range utilization. *Nanoscale* **9**, 12364–12371 (2017).
- Patrick, C. E. & Giustino, F. Structural and electronic properties of semiconductor-sensitized solar-cell interfaces. *Adv. Funct. Mater.* **21**, 4663–4667 (2011).
- Li, Z. et al. 9.2%-efficient core-shell structured antimony selenide nanorod array solar cells. *Nat. Commun.* **10**, 125 (2019).
- Deng, H. et al. Quasiepitaxy strategy for efficient full-inorganic Sb_2S_3 solar cells. *Adv. Funct. Mater.* **29**, 1901720 (2019).
- Jin, X. et al. In situ growth of [hkl]-oriented Sb_2S_3 for solution-processed planar heterojunction solar cell with 6.4% efficiency. *Adv. Funct. Mater.* **30**, 2002887 (2020).
- Qiu, Z. et al. Solution-processed solar cells based on inorganic bulk heterojunctions with evident hole contribution to photocurrent generation. *Phys. Chem. Chem. Phys.* **17**, 12328–12339 (2015).
- Lin, Y. et al. High-performance fullerene-free polymer solar cells with 6.31% efficiency. *Energy Environ. Sci.* **8**, 610–616 (2015).
- Breeze, A. J., Schlesinger, Z., Carter, S. A. & Brock, P. J. Charge transport in TiO_2 /MEH-PPV polymer photovoltaics. *Phys. Rev. B* **64**, 125205 (2001).
- Shrotriya, V., Li, G., Yao, Y., Chu, C.-W. & Yang, Y. Transition metal oxides as the buffer layer for polymer photovoltaic cells. *Appl. Phys. Lett.* **88**, 073508 (2006).
- Fan, X., Zhang, M., Wang, X., Yang, F. & Meng, X. Recent progress in organic-inorganic hybrid solar cells. *J. Mater. Chem. A* **1**, 8694–8709 (2013).
- Marchiori, C. F. N. & Koehler, M. Density functional theory study of the dipole across the P3HT:PCBM complex: the role of polarization and charge transfer. *J. Phys. D* **47**, 215104 (2014).
- Liu, C. P. et al. Enhanced performance by incorporation of zinc oxide nanowire array for organic-inorganic hybrid solar cells. *Appl. Phys. Lett.* **100**, 243102 (2012).
- Günes, S., Neugebauer, H. & Sariciftci, N. S. Conjugated polymer-based organic solar cells. *Chem. Rev.* **107**, 1324–1338 (2007).
- Thompson, B. C. & Fréchet, J. M. J. Polymer-fullerene composite solar cells. *Angew. Chem. Int. Ed.* **47**, 58–77 (2008).
- Gregg, B. A. & Hanna, M. C. Comparing organic to inorganic photovoltaic cells: theory, experiment, and simulation. *J. Appl. Phys.* **93**, 3605–3614 (2003).

35. Elumalai, N. K. & Uddin, A. Open circuit voltage of organic solar cells: an in-depth review. *Energy Environ. Sci.* **9**, 391–410 (2016).
36. Midori, K., Fukuhara, T., Tamai, Y., Kim, H. D. & Ohkita, H. Enhanced hole transport in ternary blend polymer solar cells. *ChemPhysChem* **20**, 2683–2688 (2019).
37. Zhang, F. et al. Recent development of the inverted configuration organic solar cells. *Sol. Energy Mater. Sol. Cells* **95**, 1785–1799 (2011).
38. Fabregat-Santiago, F., Garcia-Belmonte, G., Mora-Seró, I. & Bisquert, J. Characterization of nanostructured hybrid and organic solar cells by impedance spectroscopy. *Phys. Chem. Chem. Phys.* **13**, 9083–9118 (2011).
39. Kim, H.-S. et al. High efficiency solid-state sensitized solar cell-based on submicrometer rutile TiO₂ nanorod and CH₃NH₃PbI₃ perovskite sensitizer. *Nano Lett.* **13**, 2412–2417 (2013).
40. Jiang, X. et al. Template-free synthesis of vertically aligned CdS nanorods and its application in hybrid solar cells. *Sol. Energy Mater. Sol. Cells* **94**, 338–344 (2010).
41. Laban, W. A. & Egar, L. Depleted hole conductor-free lead halide iodide heterojunction solar cells. *Energy Environ. Sci.* **6**, 3249–3253 (2013).
42. Rong, Z. et al. Interface engineering for both cathode and anode enables low-cost highly efficient solution-processed CdTe nanocrystal solar cells. *Adv. Funct. Mater.* **29**, 1904018 (2019).
43. Kirchartz, T. et al. Sensitivity of the Mott-Schottky analysis in organic solar cells. *J. Phys. Chem. C* **116**, 7672–7680 (2012).
44. Bisquert, J. et al. Band unpinning and photovoltaic model for P3HT:PCBM organic bulk heterojunctions under illumination. *Chem. Phys. Lett.* **465**, 57–62 (2008).
45. Zonno, I., Martinez-Otero, A., Hebig, J.-C. & Kirchartz, T. Understanding Mott-Schottky measurements under illumination in organic bulk heterojunction solar cells. *Phys. Rev. Appl.* **7**, 034018 (2017).
46. Tait, J. G. et al. Interfacial depletion regions: beyond the space charge limit in thick bulk heterojunctions. *ACS Appl. Mater. Interfaces* **8**, 2211–2219 (2016).
47. Bisquert, J. & Vikhrenko, V. S. Interpretation of the time constants measured by kinetic techniques in nanostructured semiconductor electrodes and dye-sensitized solar cells. *J. Phys. Chem. B* **108**, 2313–2322 (2004).
48. Bouclé, J. et al. Hybrid solar cells from a blend of poly(3-hexylthiophene) and ligand-capped TiO₂ nanorods. *Adv. Funct. Mater.* **18**, 622–633 (2008).

Acknowledgements

This work was supported by the National Natural Science Foundation of China (grant nos. 11474286, 61704048, 11974353, 52002373), the Collaborative Innovation Program of Hefei Science Center, CAS (grant no. 2020HSC-CIP004), the HFIPS President Foundation (grant no. YZJZX202018), and the Program for Science and Technology Innovation Talents in Universities of Henan Province (grant no. 19HASTTT049).

Author contributions

R.L., Z.S., and Z.W. contributed equally to this work. R.L. designed and performed the NHJ synthesis, solar cell fabrication, and sample characterizations. Z.S. and C.C. conducted the DFT calculations and the related analyses. Z.W. performed the EIS and C–V measurements. L. Zhu helped to prepare the NHJ samples. J. Chen contributed to the design of the NHJ synthesis. C.D., W.C., and W.C. helped to prepare the solar cells. B.C., X.Y. and B.D. contributed to the simulations and analyses using COMSOL Multiphysics software. S.Y., T.C. and X.T. helped with the solar cell characterization. M.W. conceived the study and supervised the project. M.W. and R.L. analyzed the data, interpreted the results, and prepared the manuscript. All authors read and edited the manuscript.

Competing interests

The authors declare no competing interests.

Additional information

Supplementary information The online version contains supplementary material available at <https://doi.org/10.1038/s42005-021-00678-1>.

Correspondence and requests for materials should be addressed to J.C., C.C. or M.W.

Peer review information *Communications Physics* thanks the anonymous reviewers for their contribution to the peer review of this work. Peer reviewer reports are available.

Reprints and permission information is available at <http://www.nature.com/reprints>

Publisher's note Springer Nature remains neutral with regard to jurisdictional claims in published maps and institutional affiliations.



Open Access This article is licensed under a Creative Commons Attribution 4.0 International License, which permits use, sharing, adaptation, distribution and reproduction in any medium or format, as long as you give appropriate credit to the original author(s) and the source, provide a link to the Creative Commons license, and indicate if changes were made. The images or other third party material in this article are included in the article's Creative Commons license, unless indicated otherwise in a credit line to the material. If material is not included in the article's Creative Commons license and your intended use is not permitted by statutory regulation or exceeds the permitted use, you will need to obtain permission directly from the copyright holder. To view a copy of this license, visit <http://creativecommons.org/licenses/by/4.0/>.

© The Author(s) 2021